Supplementary Materials

Suppressing charge recombination in a methylammonium-free wide-bandgap perovskite film for high-performance and stable perovskite solar cells

Qiufeng Ye, ‡[a,c] Wenzheng Hu, ‡[a] Junchi Zhu,[a] Ziyu Cai,[a] Hengkang Zhang,[a] Tao Dong,[a] Boyang Yu,[a] Feiyang Chen,[a] Xieli Wei,[a] Bo Yao,[a] Weidong Dou,[a] Zebo Fang,*[a] Feng Ye,*[b] Zhun Liu,*[a] Tie Li*[c]

[a]Department of Physics and Zhejiang Engineering Research Center of MEMS, Shaoxing University, Shaoxing 312000, P. R. China.

　　Email: yeqiufeng21@usx.edu.cn, csfzb@usx.edu.cn, liu6zhun@163.com

[b]Shangyu Coll, Shaoxing University, Shaoxing 312300, P. R. China.

　　Email: yefeng@usx.edu.cn

[c]Science and Technology on Microsystem Laboratory, Shanghai Institute of Microsystem and Information Technology, Chinese Academy of Sciences, Shanghai 200050, P. R. China.

　　Email: tli@mail.sim.ac.cn

Materials

The SnO_2 nanoparticle precursor was purchased from Alfa Aesar (tin (IV) oxide, 15% in H_2O colloidal dispersion). Formamidinium iodide (FAI) and methylammonium chloride (MACl), The Cesium iodide (CsI) was purchased from Aladdin. 2,2′,7,7′-tetrakis(N,N-di-p-methoxyphenylamine)-9,9′-spirobifluorene (Spiro-OMeTAD), lithium bis (trifluoromethanesulfonyl) imide (LiTFSI) were purchased from Xi'an Polymer Light Technology. The Lead bromide ($PbBr_2$) was obtained from Shanghai Macklin Biochemical Co., Ltd. N,N-dimethylmethanamide (DMF, 99.9%), dimethyl sulfoxide (DMSO, 99.9%), 4-t-butylphenylammonium iodide (tBP), acetonitrile (ACN) and Chlorobenzene (CB) were purchased from Advanced Election Technology Co., Ltd. Trioctylphosphine oxide (TOPO, 99%), Isopropanol (IPA) and Lead iodine (PbI_2, 99.999%) were purchased from Sigma-Aldrich.

Wide-bandgap perovskite precursor preparation

In 1 milliliter of mixed DMF and DMSO (v/v = 4:1) solvents, 178.78 mg of FAI, 67.6 mg of CsI, 374.56 mg of PbI_2, 178.91 mg of $PbBr_2$, and 32.67 mg of MACl were mixed to form the 1.3 M wide-bandgap perovskite precursor solution of $FA_{0.8}Cs_{0.2}Pb(I_{0.75}Br_{0.25})_3$. The optimized solution was mixed with RbI (2 mg, 4 mg, 6 mg) and stirred for 6 hours before using.

Wide-bandgap perovskite solar cell fabrication

The ITO substrates were subjected to a cleaning process involving conductive glass cleaning agent, DI water, acetone, and isopropanol for 20 minutes using ultrasonic processing. Subsequently, the ITO substrate underwent UVO treatment for 20 minutes. Following this, the SnO_2 nanoparticle solution (with a

ratio of SnO$_2$ nanoparticle solution to DI water of 1:3) was spin-coated onto the substrate at 4000 rpm for 30 seconds and annealed at 150 °C for 30 minutes in dry air. After cooling to room temperature, the SnO$_2$ substrates were placed in UVO for 10 minutes. The FA$_{0.83}$Cs$_{0.17}$Pb(I$_{0.75}$Br$_{0.25}$)$_3$ precursor was spin-coated onto the SnO$_2$ film at 1000 rpm for 10 seconds, followed by 5000 rpm for 35 seconds, and then 200 μl of CB was rapidly dropped onto the rotating film in the last 5 seconds. Subsequently, the film was immediately annealed in air for ten minutes. Then, 30 μL of FAI solution (4 mg/ml in IPA) was dropped onto the perovskite film at 3000 rpm for 30 seconds and annealed at 100 °C for 10 minutes to construct surface heterojunction (SHJ). Following this, 30 μL of TOPO (1 mg/ml in IPA) was spin-coated onto the SHJ film at 3000 rpm for 30 seconds. The hole transporting layer was then prepared by spin-coating a mixture solution of Spiro-OMeTAD (72.3 mg), Li-TSFI (35 μL) solution (260 mg Li-TSFI in 1 ml ACN), and tBP (30 μL) in CB (1 mL) onto the film. Finally, 50 nm of gold was evaporated onto the top to serve as electrodes. The size areas of small-scale device were 0.0441 cm^2, a 0.0404 cm^2 non-reflective mask was used to define the accurate active cell area while measuring. And the size areas of large-scale device were 1.210 cm^2, and a 1.02 cm^2 non-reflective mask was used to define the accurate active cell area while measuring.

Relative narrow-bandgap (~1.55 eV) perovskite solar cell preparation

We applied two-step sequential deposition method to fabricate the ~1.55 eV PSCs. The substrate cleaning and preparation technology of electron transport layer SnO$_2$ is consistent with the above method. After that, 1.5 M of PbI$_2$ in (DMF:DMSO = 9.5: 0.5) was spin coated onto SnO$_2$ at 1500 rpm for 30 s, and then annealed at 70 °C for 1 min, then the mixture solution of FAI: MAI: MACl (90 mg: 9 mg: 9 mg in 1 ml IPA) was spin coated onto the PbI$_2$ at spin rate ranging of 2000 rpm for 30 s, and a thermal annealing of 150 °C for 15 min in ambient air condition (30–40% humidity) was processed. Following this, 30 μL of TOPO (1 mg/ml in IPA) was spin-coated onto the SHJ film at 3000 rpm for 30 seconds. The hole transporting layer Spiro-OMeTAD was then prepared by spin-coating onto the film. Finally, 50 nm of gold was evaporated onto the top to serve as electrodes.

Simulation method

The numerical calculation was performed by a one-dimensional simulator as implemented in the Solar Cell Capacitance Simulator program (SCAPS, developed by the University of Gent) that solves the equations governing the behavior of semiconductor materials in steady state conditions, including the Poisson equation, electron and hole continuity equations, drift and diffusion currents equation. Originally, the program was developed specifically for analyzing cell structures made of CuInSe$_2$ and the CdTe family. However, recent advancements have expanded the program's capabilities to include the analysis of crystalline solar cells from the Si and GaAs family, as well as perovskite solar cells. We, therefore, applied this device simulator to analyze the impact of various parameters on the performance of perovskite solar cells.

The Poisson equation describes the relationship between the electric field (E)and the space charge density (ρ):

$$\frac{\partial^2 \psi}{\partial^2 x} = -\frac{\partial E}{\partial x} = -\frac{\rho}{\varepsilon_s} = -\frac{q}{\varepsilon_s}[p - n + N_D^+(x) - N_A^-(x) \pm N_{def}(x)] \qquad (1)$$

Where, Ψ is the electrostatic potential, q is the elementary charge, ε_s is the static relative permittivity of the medium, $n(p)$ is the electron (hole) density, $N_D^+(N_A^-)$ is the density of ionized donors (acceptors), and N_{def} is the possible defect (Acceptor or donor) density.

The electron and hole continuity equations in steady state are given by:

$$\frac{\partial J_n}{\partial x} + G - U_n(n, p) = 0 \tag{2}$$

$$-\frac{\partial J_p}{\partial x} + G - U_p(n, p) = 0 \tag{3}$$

J_n, J_p are the electron and hole current densities; $U_{n(p)}$ is the net recombination rates; G is the electron-hole generation rates.

Under the influence of an electric field, a few carriers will experience drift, leading to the occurrence of the drift phenomenon. Additionally, there will be the generation of diffusion current due to the concentration gradient. The relationship between drift and diffusion currents is given by the continuity equation:

$$J_n = qnu_nE + qD_n\nabla n \tag{4}$$

$$J_p = qnu_pE + qD_p\nabla p \tag{5}$$

q is the elementary charge, U_n is electron mobility, U_p is hole mobility, and D_n is the diffusion coefficient of electrons, D_p is the diffusion coefficient of holes.

The equations for calculating short-circuit current and open-circuit voltage are as follows:

$$J_{sc} = q\int \frac{\lambda}{hc} QE(\lambda) I_{AM1.5}(\lambda) d\lambda \tag{6}$$

$$V_{oc} = \frac{mk_BT}{q} ln(\frac{J_{sc}}{J_m^0} + 1) \tag{7}$$

$I_{AM1.5}(\lambda)$ is the illumination amplitude at wavelength, c is the speed of light, h is the Planck constant. J_m^0 is reverse saturated non-ideal diode current, m is ideal factor, and T is temperature.

The FF is calculated as follows:

$$FF = \frac{J_{Mp}V_{Mp}}{J_{sc}V_{oc}} \tag{8}$$

Here, J_{Mp} and V_{Mp} are the current density and voltage at the maximum power points. Efficiency η, normalized to input power, P_{in} is defined as:

$$\eta = \frac{V_{oc}.J_{sc}.FF}{P_{in}} \tag{9}$$

Device characterization

A 3Kv field-emission scanning electron microscope (Zeiss Sigma300) was used to take the SEM characterization images of the films. The positions of the perovskite crystal peaks (Rigaku S3 D/MAX-2400) were ascertained by XRD investigation. Using a Varian Cary 5000 spectrophotometer, the UV absorption characteristics of perovskite films were determined. AFM (Bruker Multimode8) was used to

assess the film's surface roughness, and SEM (Zeiss Sigma300) was used to determine the device's cross-section shape. Utilizing PL spectral equipment (FLS980 spectrometer (UK)) and time-resolved PL spectral equipment (F900 spectrometer (UK)), the carrier lifetime data of the thin films were acquired. By utilizing the Keithley 2400 source measurement unit, the J-V characteristics of perovskite solar cells were analyzed. The measurements were carried out under a simulated AM 1.5 G spectrum (Newport 94023A S/N:525). Within a nitrogen glove box, both reverse scan (1.4 V→0 V, step 0.02 V) and forward scan (0 V→1.4 V, step 0.02 V) were conducted on the photovoltaic cells. The Thermo Scientific ESCALab 250Xi instrument, powered by 200 W monochromated Al Kα (1486.6 eV) radiation, was utilized to acquire the EDS data. Employing HeI (21.22 eV) radiation lines, Ultraviolet photoelectron spectroscopy (UPS) spectra were acquired using the Thermo Scientific ESCALab 250Xi instrument.
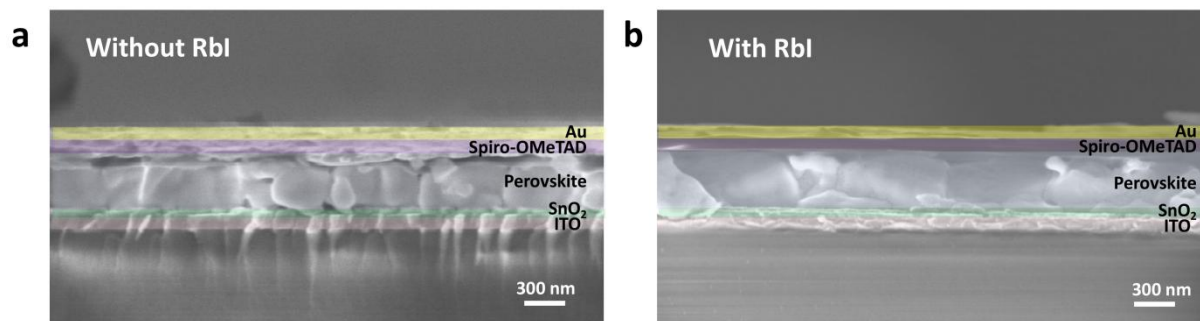
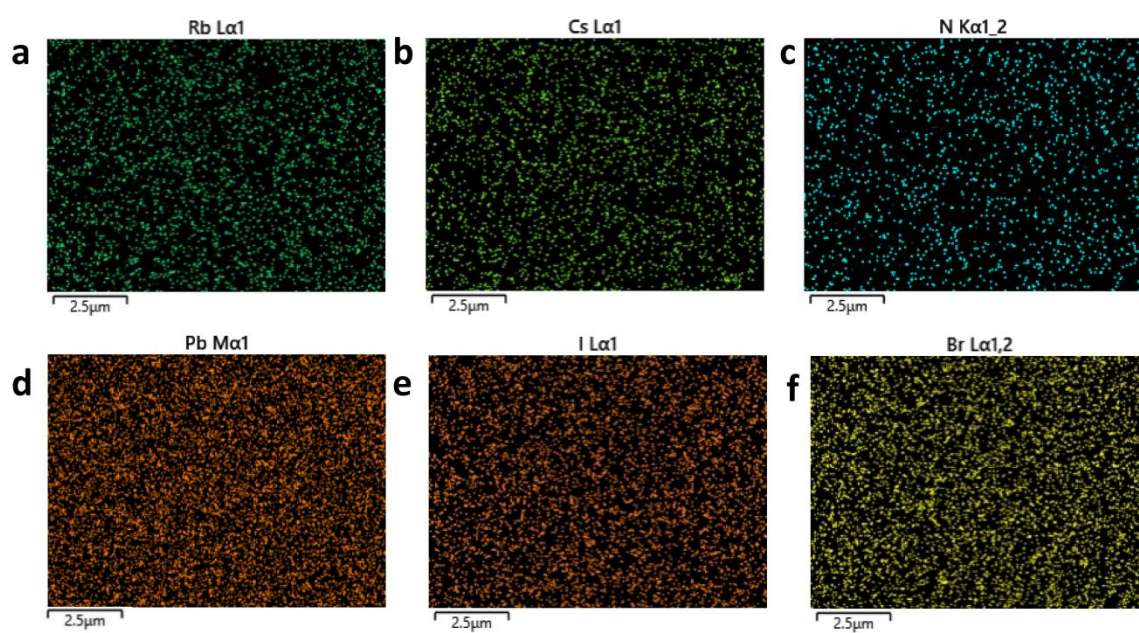**Fig. S1.** Cross-sectional SEM of the WBG solar cells without/with RbI.

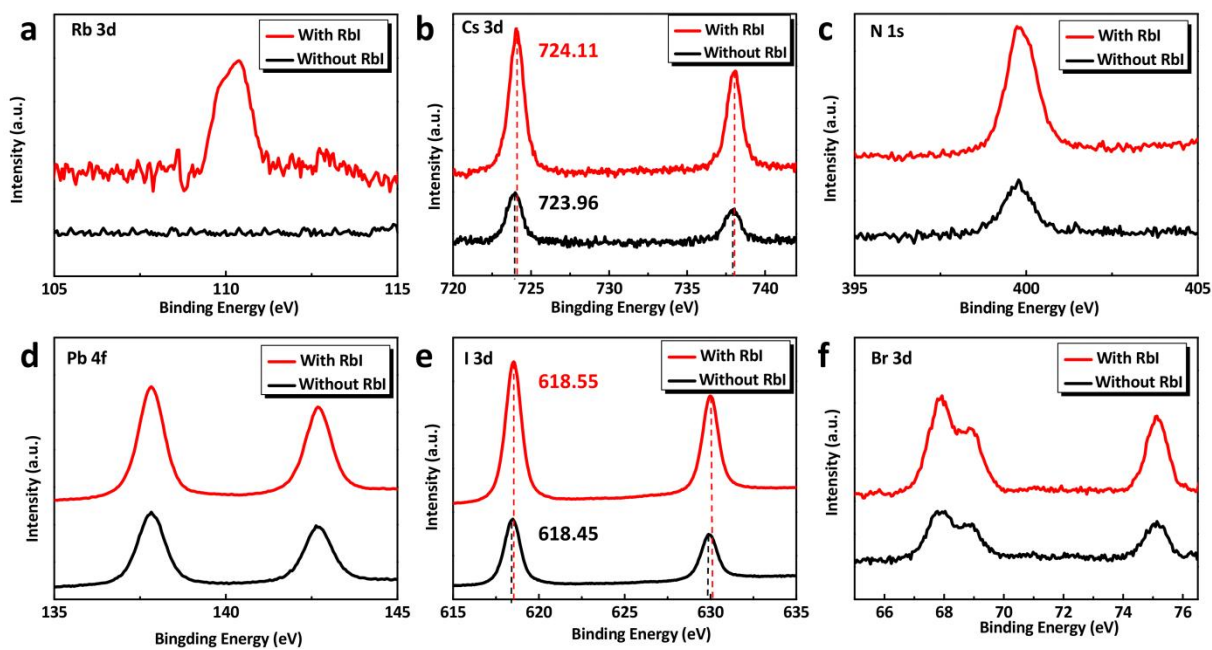**Fig. S2.** EDS of perovskite films with RbI.

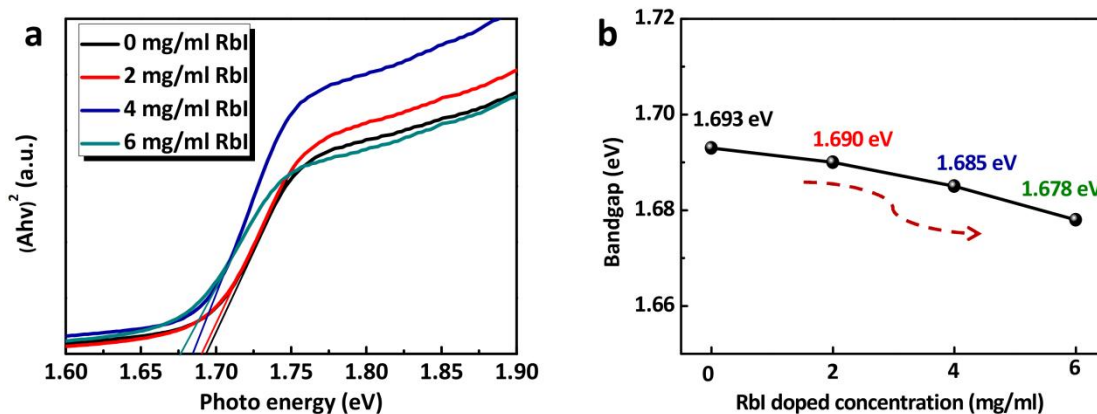**Fig. S3.** XPS of perovskite films without/with RbI.

Fig. S4. a) The corresponding bandgap calculated with Tauc equation of the WBG perovskite films doped with different concentrations of RbI. b) The bandgaps statistics of the WBG perovskite films doped with different concentrations of Rb
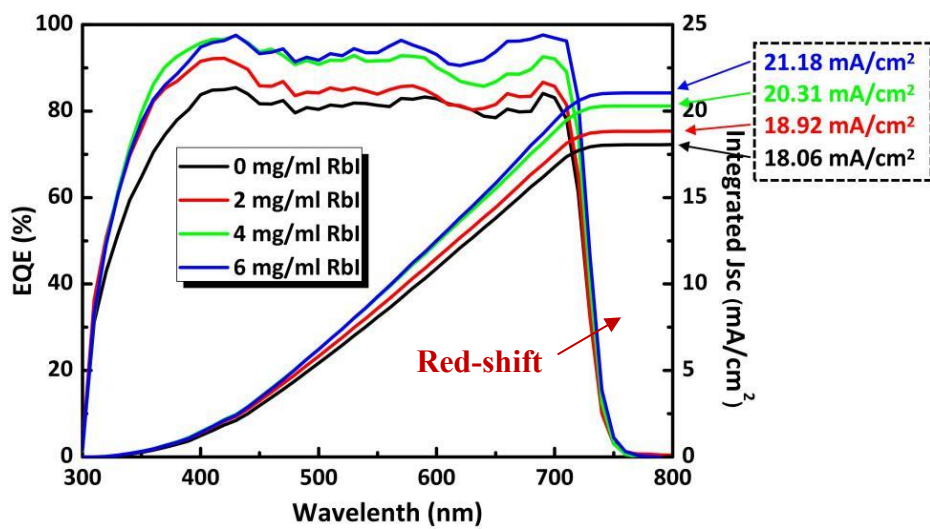
Fig. S5. The EQE spectra of the WBG solar cells with different concentrations of RbI.
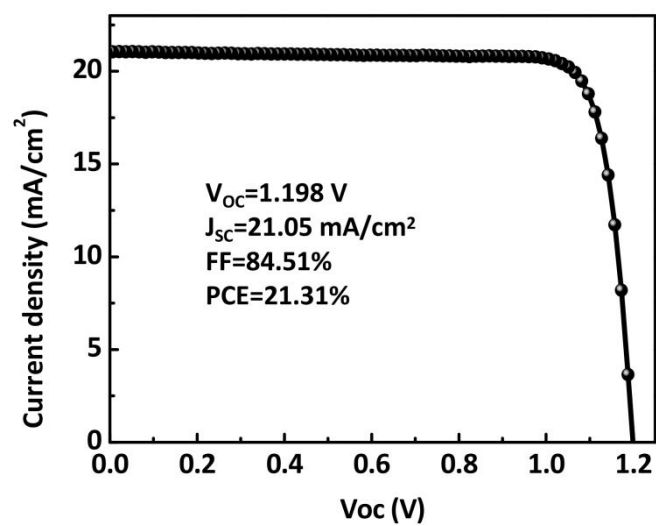
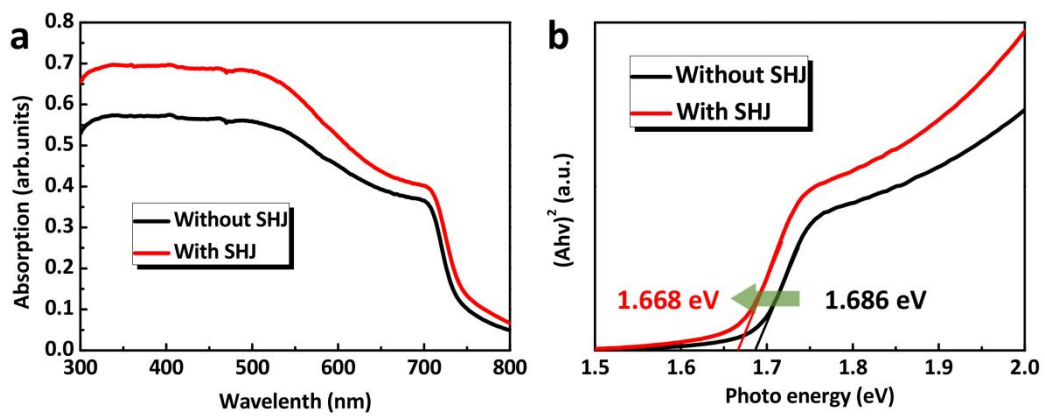**Fig. S6.** J-V curves of RbI optimized p-i-n inverted PSCs.

Fig. S7. a) UV-vis absorption spectra and b) The corresponding bandgap calculated with Tauc equation of the perovskite films without/with SHJ.
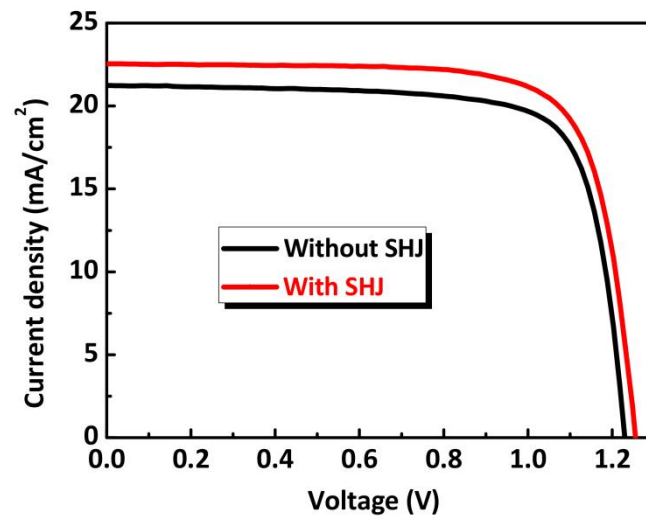
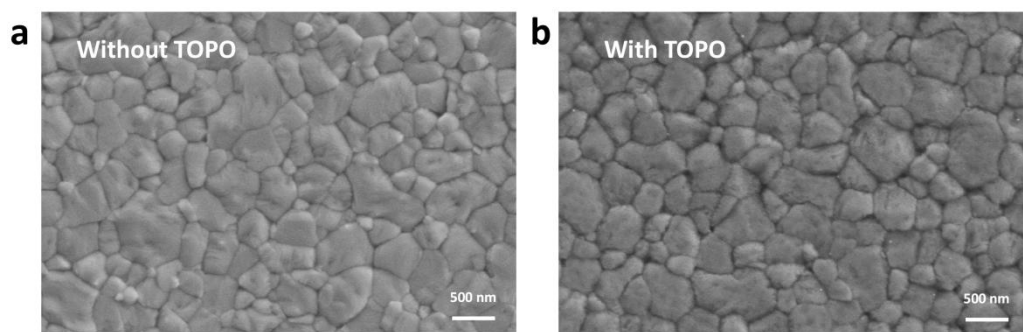**Fig. S8.** Illuminated J-V curves of the WBG solar cell devices without/with SHJ.

Fig. S9. SEM images of without and with TOPO passivated perovskite film.
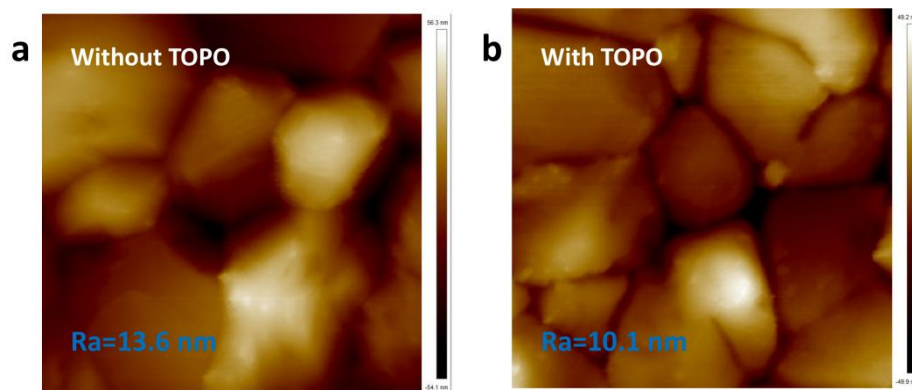
Fig. S10. AFM images of without and with TOPO passivated perovskite film.
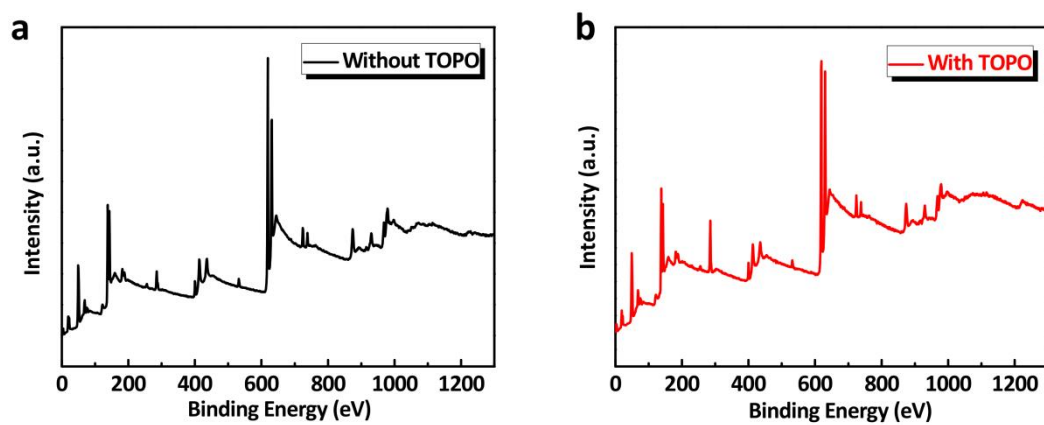
Fig. S11. XPS full spectra of the perovskite films without/with TOPO.
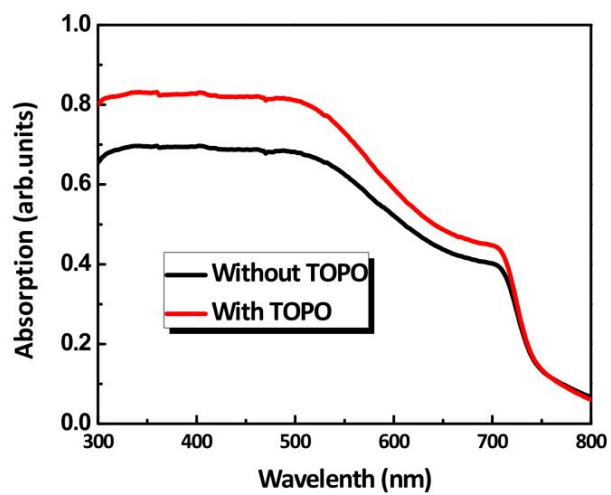
Fig. S12. UV-vis absorption spectra without and with TOPO passivated perovskite film.
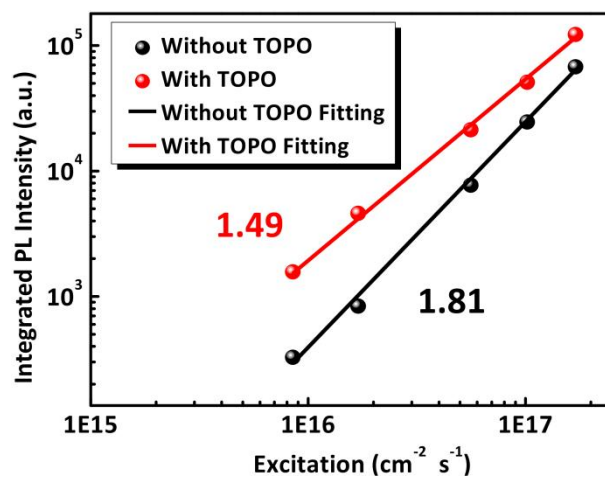
Fig. S13. The fluence intensity dependence of PL spectra for the WBG perovskite films with and without TOPO (assuming that 1-sun equivalent fluence for 1.685-eV bandgap is about 1.90×10^{17} photons $cm^{-2} s^{-1}$).
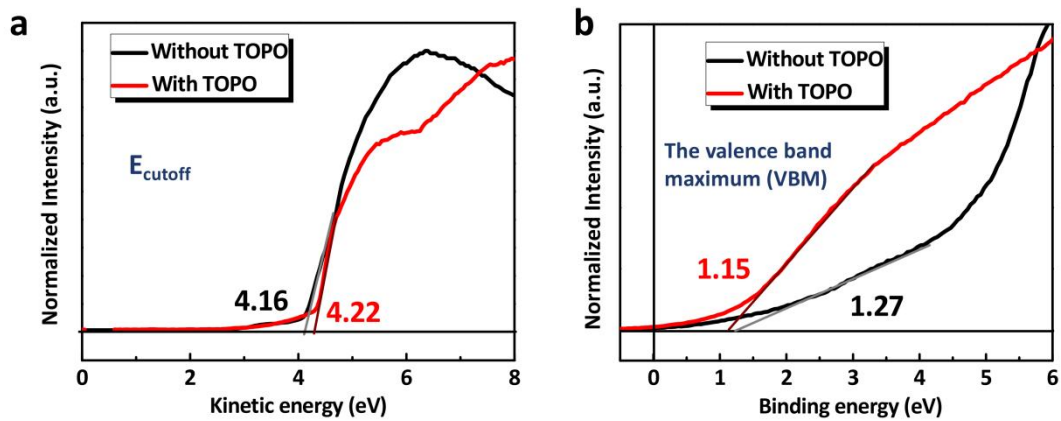
Fig. S14. UPS spectra of the perovskite films without/with TOPO.
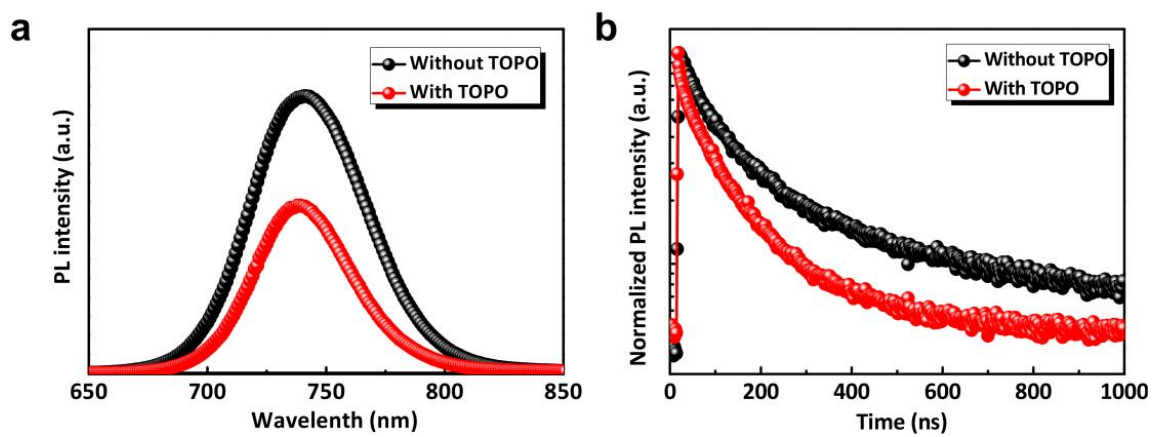
Fig. S15. The Charge transport properties between perovskite layer and Spiro-OMeTAD with and without TOPO passivation (a) PL spectra. (b) TRPL spectra.
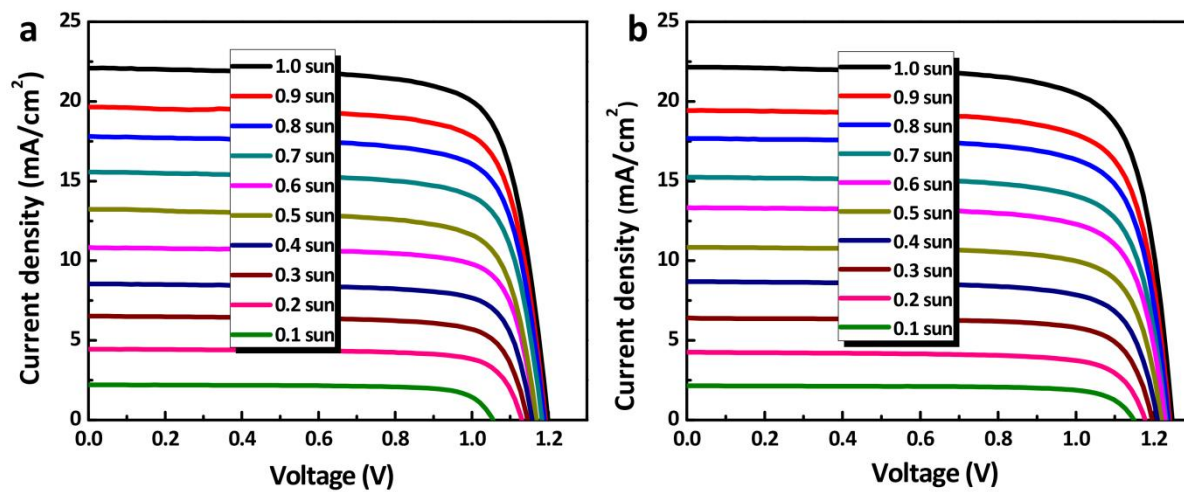
Fig. S16. J-V curves of without and with TOPO passivated PSCs   at different light intensity (0.1-1 sun).
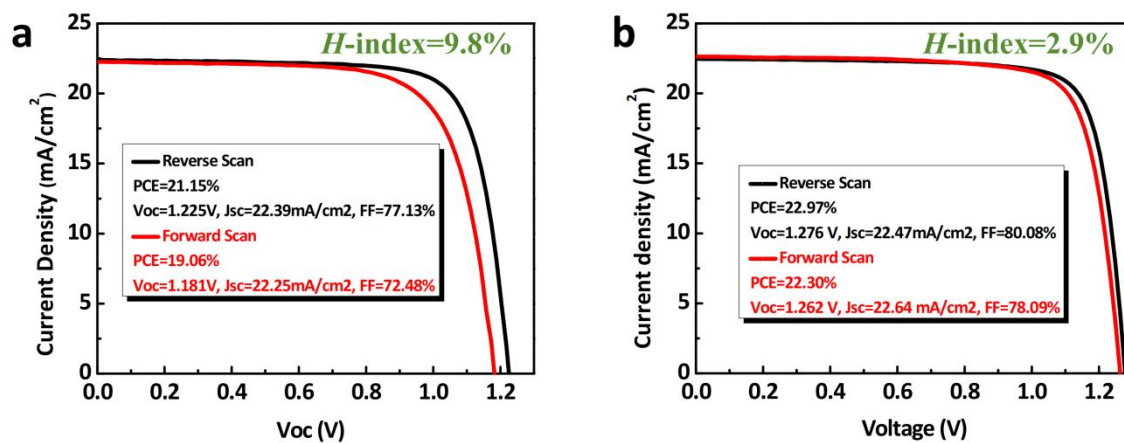
Fig. S17. The J-V hysteresis study of without and with TOPO passivated PSCs.
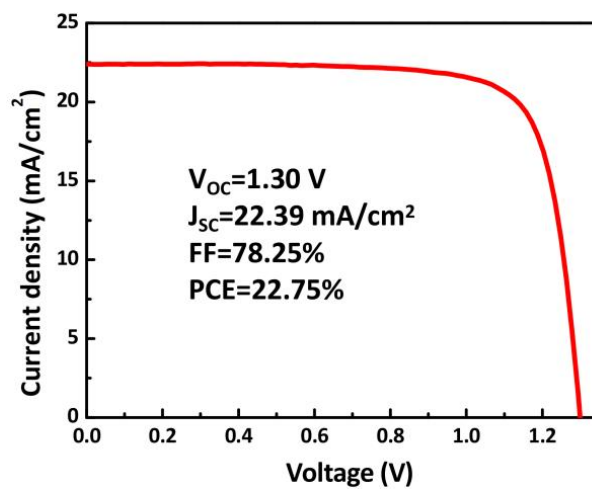
Fig. S18. The J-V curve of TOPO passivated WBG PSCs with a high V_{OC} of 1.30 V.
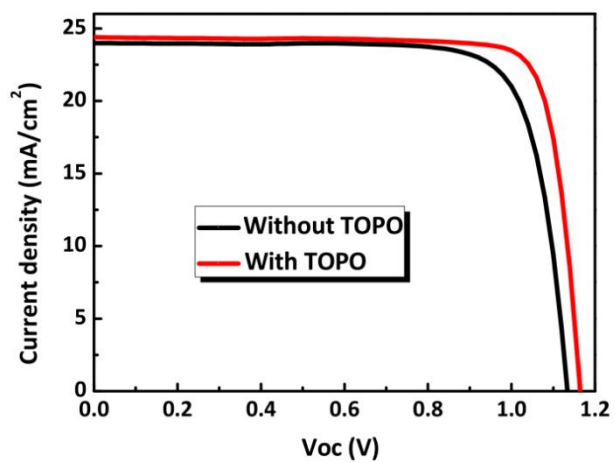
Fig. S19. J-V curves of TOPO passivated PSCs with the bandgap of 1.55 eV.
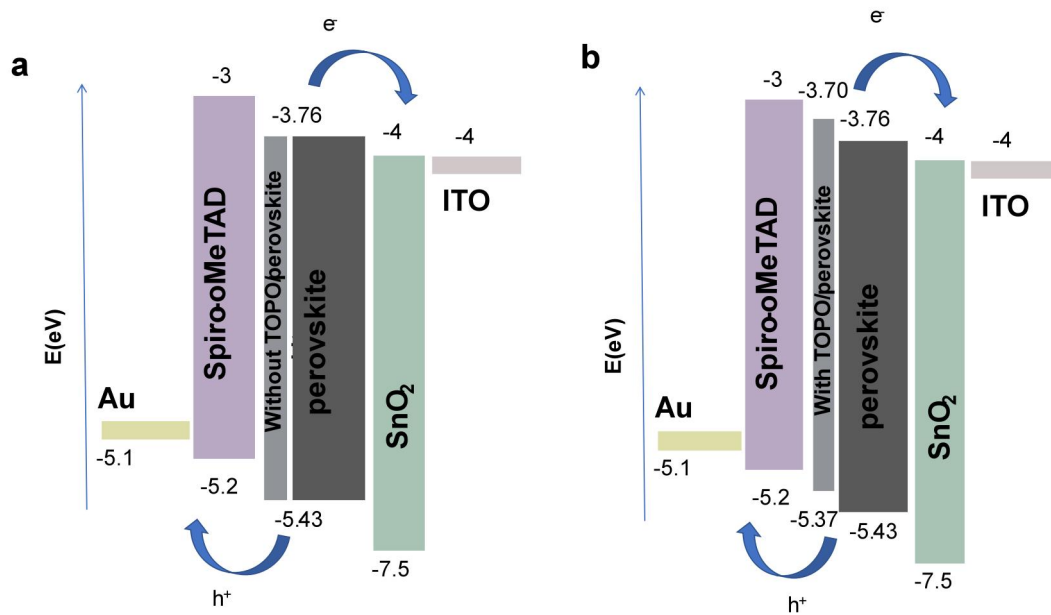
Fig. S20. Energy level of each layer in the PSCs a) without TOPO b) with TOPO treated devices.
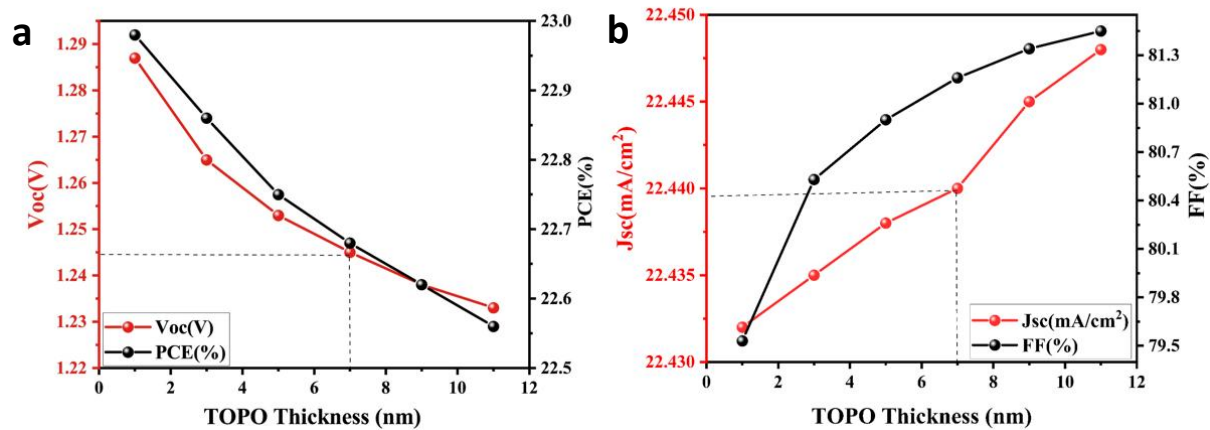
Fig. S21. Influence of TOPO with different thicknesses a) on Voc and PCE b) Jsc and FF.

Sample	V_{OC} (V)	J_{SC} (mA/cm²)	FF (%)	PCE (%)
w/o band offset	1.245	22.44	78.30	21.87
w/ band offset	1.245	22.44	81.16	22.68
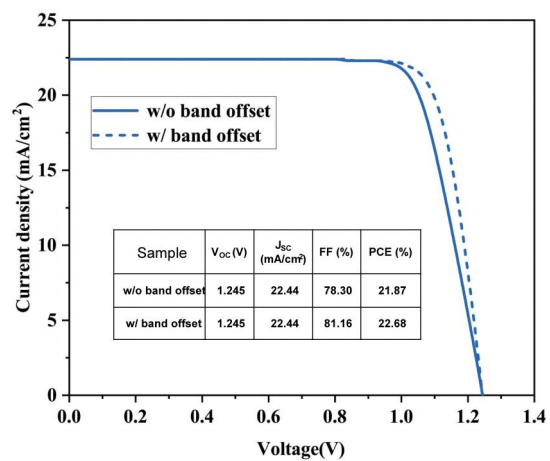
Fig. S22. J-V curve analysis without band offset (typical device) and with up-shifted band offset in the device (TOPO passivated).
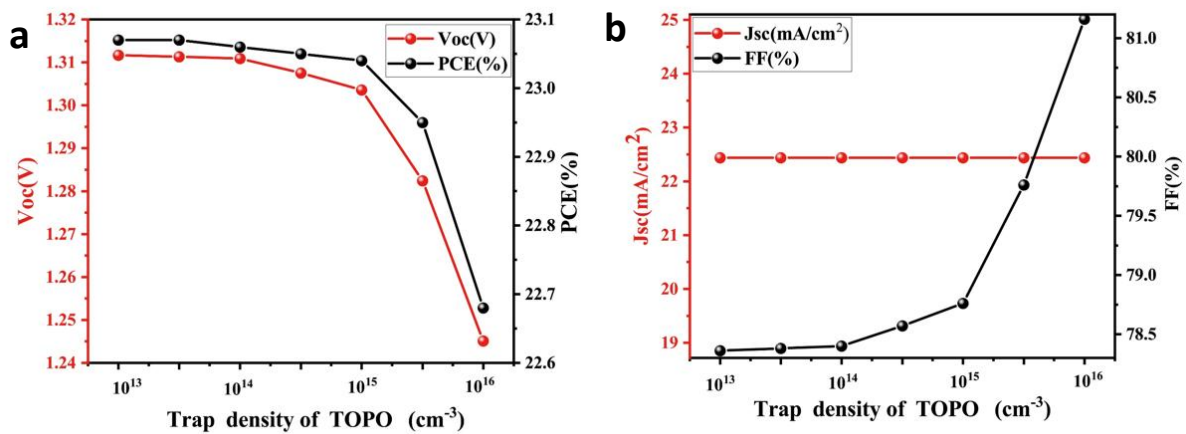
Fig. S23. Influence of TOPO different trap density a) on Voc and PCE b) Jsc and FF.
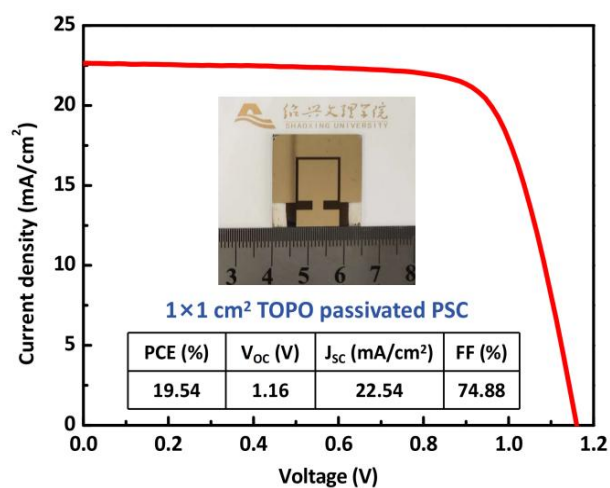
Fig. S24. J-V curves of TOPO passivated PSCs with the large area (1 cm^2).

Table S1. Fitted fast and slow decay components for the TRPL measurements of perovskite films with different concentrations of RbI.

Sample	$\tau 1$ (ns)	$\tau 2$ (ns)	A1 (%)	A2 (%)	$\tau_{average}$ (ns)
Without RbI	2.5	69.4	4.2	95.8	66.6
2 mg/ml RbI	3.6	92.2	4.3	95.7	88.4
4 mg/ml RbI	5.2	156.8	5.6	94.4	148.1
6 mg/ml RbI	4.3	106.4	4.8	95.2	101.5

Table S2. Photovoltaic performance of the WBG solar cell devices doped with different concentrations of RbI.

Sample	V_{OC} (V)	J_{SC} (mA/cm^2)	FF (%)	PCE (%)
0 mg/ml RbI	1.164	18.98	69.22	15.29
2 mg/ml RbI	1.189	20.34	73.78	17.84
4 mg/ml RbI	1.233	21.46	76.01	20.11
6 mg/ml RbI	1.204	21.69	73.64	19.24

Table S3. Photovoltaic performance of the WBG solar cell devices without and with SHJ.

Sample	V_{OC} (V)	J_{SC} (mA/cm²)	FF (%)	PCE (%)
Without SHJ	1.229	21.25	76.58	19.98
With SHJ	1.254	22.53	76.13	21.52

Table S4. Fitted fast and slow decay components for the TRPL measurements of perovskite films without and with TOPO passivated.

Sample	$\tau 1$ (ns)	$\tau 2$ (ns)	A1 (%)	A2 (%)	$\tau_{average}$ (ns)
Without TOPO	103.7	393.7	48.0	52.0	242.9
With TOPO	326.8	1072.0	47.3	52.7	679.3

Table S5. A summary of the detail performance parameters of reported WBG PSCs in this work and in the literatures.

System	Year	V_{OC}	PCE	Perovskite Component	Eg	V_{OC} deficits	Ref
MA System	2016	1.24	21.6	$Rb_{0.05}(Cs_{0.05}MAFA)_{0.95}Pb(I_{0.83}Br_{0.17})_3$	1.63	0.39	[1]
	2016	1.04	12.59	$MAPb_{0.75}Sn_{0.25}(I_{0.4}Br_{0.6})_3$	1.73	0.69	[2]
	2017	1.15	17.2	$FA_{0.83}MA_{0.17}Pb(I_{0.6}Br_{0.4})_3$	1.72	0.57	[3]
	2018	1.146	16.0	$FA_{0.4}Cs_{0.5}MA_{0.1}Pb(I_{0.83}Br0._{17})_3$	1.699	0.553	[4]
	2018	1.25	19.3	$FA_{0.83}Cs_{0.12}MA_{0.05}Pb(I_{0.6}Br_{0.4})_3$	1.74	0.49	[5]
	2020	1.26	18.38	$KI\text{-}Cs_{0.05}MA_{0.16}FA_{0.79}Pb(I_{0.75}Br_{0.25})_3$	1.75	0.49	[6]
	2020	1.196	21.0	$(FA_{0.64}MA_{0.20}Cs_{0.15})Pb_{0.99}(I_{0.79}Br_{0.2})_3$	1.68	0.484	[7]
	2022	1.22	22.28	$(CsMAFA)Pb(I, Br)_3$	1.67	0.45	[8]
	2023	1.20	23.23	$(CsMAFA)Pb(I, Br)_3$	1.63	0.43	[9]
DMA System	2019	1.20	19.2	$FA_{0.6}Cs_{0.3}DMA_{0.1}Pb(I_{0.8}Br_{0.2})_3$	1.7	0.5	[10]
	2022	1.33	20.1	$Cs_{0.3}FA_{0.6}DMA_{0.1}Pb(I_{0.7}Br_{0.3})_3$	1.75	0.48	[11]
MA Free System	2016	1.20	17.1	$FA_{0.83}Cs_{0.17}Pb(I_{0.6}Br_{0.4})_3$	1.74	0.54	[12]
	2017	1.24	18.1	$FA_{0.15}Cs_{0.85}Pb(I_{0.73}Br_{0.27})_3$	1.72	0.48	[13]
	2017	1.25	18.27	$FA_{0.8}Cs_{0.2}Pb(I_{0.7}Br_{0.3})_3$	1.75	0.5	[14]
	2018	1.23	17.8	$FA_{0.83}Cs_{0.17}Pb(I_{0.6}Br_{0.4})_3$	1.75	0.52	[15]
	2018	1.22	20.7	$Cs_{0.2}FA_{0.8}Pb(I_{0.75}Br_{0.25})_3$	1.65	0.5	[16]
	2019	1.24	18.19	$FA_{0.8}Cs_{0.2}Pb(I_{0.7}Br_{0.3})_3$	1.75	0.51	[17]
	2020	1.197	16.4	$FA_{0.8}Cs_{0.2}Pb(I_{0.6}Br_{0.4})_3$	1.77	0.573	[18]
	2021	1.19	20.31	$FA_{0.8}Cs_{0.2}Pb(I_{0.8}Br_{0.2})_3$	1.68	0.49	[19]
	2022	1.22	17.0	$FA_{0.83}Cs_{0.17}Pb(I_{0.6}Br_{0.4})_3$	1.79	0.57	[20]
	2023	1.25	19.66	$Cs_{0.2}FA_{0.8}Pb(I_{0.6}Br_{0.4})_3$	1.77	0.52	[21]
	2024	1.30	**23.35**	$FA_{0.8}Cs_{0.2}Pb(I_{0.75}Br_{0.25})_3$	1.685	**0.385**	**This work**

Table S6. Photovoltaic performance of the narrow bandgap (1.55 eV) solar cell devices without and with TOPO.

Sample	V_{OC} (V)	J_{SC} (mA/cm^2)	FF (%)	PCE (%)
Without TOPO	1.133	23.98	78.76	21.57
With TOPO	1.162	24.38	83.09	23.50

Table S7. The listed materials are used for the simulation of the device, and all the parameters related to its electrical and optical properties were taken from published references.[22-26]

Material Parameters	HTL	TOPO	Perovs kite	ETL	ITO
Thickness(nm)	150	7	Variable	50	200
Bandgap, Eg(eV)	3.0	1.668	1.668	3.5	3.5
Electron affinity, χ(eV)	2.2	3.76/3.70	3.76	4.0	4
Dielectric permittivity, ε_r	3	6.5	6.5	9	9
CB effective density of states, Nc(cm^{-3})	2.8×10^{19}	2.8×10^{18}	2.8×10^{18}	2.2×10^{18}	2.2×10^{18}
VB effective density of states, Nv((cm^{-3})	1.0×10^{19}	1.8×10^{19}	1.8×10^{19}	1.8×10^{19}	1.8×10^{18}
Electron thermal velocity(cm/s)	1×10^7	1×10^7	1×10^7	1×10^7	1×10^7
Hole thermal velocity(cm/s)	1×10^7	1×10^7	1×10^7	1×10^7	1×10^7
Electron mobility, μ_n (cm^2/Vs)	1.2×10^{-4}	20	20	1.0×10^2	2
Electron mobility, μ_p (cm^2/Vs)	2.0×10^{-4}	10	20	10	1
Shallow donor density, ND (cm^{-3})	0	0	0	1.0×10^{17}	2.0×10^{19}
Shallow acceptor density, NA (cm^{-3})	2.0×10^{18}	Variable	0	0	0
Defect density, Nt(cm^{-3})	1.0×10^{15}	Variable	5.0×10^{13}	1.0×10^{14}	1.0×10^{14}

The electron and hole trapping cross section of the perovskite layer and the TOPO layer are 10-15 cm^2. The characteristic energy of each layer is 0.1 eV, and the defect state of perovskite absorption layer accords with Gaussian neutral distribution. The reference defect energy level in the TOPO and perovskite layer is 0.65 eV above the valance band. The energy level with respect to the reference of hole transport layer, electron transport layer and ITO is 0.6 eV. The metal work function of the left and right working contact points are 5.1 eV and 4.4 eV.

Table S8. The storage stability of the TOPO passivated solar cell in ultra dry air (25 $\pm$ 3 ℃, relative humidity (RH) of $\approx$10%) and in dark.

Storage time (hours)	V_{OC} (V)	J_{SC} (mA/cm^2)	FF (%)	PCE (%)
0	1.275	22.59	79.22	22.82
144	1.277	22.48	78.32	22.49
264	1.276	22.52	77.75	22.32
360	1.272	22.61	77.32	22.24
504	1.269	22.63	76.94	22.09
672	1.269	22.64	76.62	22.01
816	1.267	22.58	76.32	21.84
1008	1.265	22.67	76.01	21.79
1320	1.265	22.57	75.92	21.71
1632	1.265	22.43	76.33	21.66
1872	1.263	22.55	75.84	21.60
2556	1.262	22.64	75.35	21.53
3408	1.260	22.68	75.29	21.48

Reference

1. M. Saliba, T. Matsui, K. Domanski, J.-Y. Seo, A. Ummadisingu, S. M. Zakeeruddin, J.-P. Correa-Baena, W. R. Tress, A. Abate, A. Hagfeldt and M. Grätzel, *Science*, 2016, **354**, 206–209.
2. Z. Yang, A. Rajagopal, S. B. Jo, C.-C. Chueh, S. Williams, C.-C. Huang, J. K. Katahara, H. W. Hillhouse and A. K.-Y. Jen, *Nano Lett.*, 2016, **16**, 7739–7747.
3. X. Zheng, B. Chen, J. Dai, Y. Fang, Y. Bai, Y. Lin, H. Wei, X. C. Zeng and J. Huang, *Nature Energy*, 2017, **2**, 1–9.
4. L. Gil-Escrig, C. Momblona, M.-G. La-Placa, P. P. Boix, M. Sessolo and H. J. Bolink, *Adv. Energy Mater.*, 2018, **8**, 1703506.
5. H. Tan, F. Che, M. Wei, Y. Zhao, M. I. Saidaminov, P. Todorović, D. Broberg, G. Walters, F. Tan, T. Zhuang, B. Sun, Z. Liang, H. Yuan, E. Fron, J. Kim, Z. Yang, O. Voznyy, M. Asta and E. H. Sargent, *Nat. Commun.*, 2018, **9**, 3100.
6. L. Wang, G. Wang, Z. Yan, J. Qiu, C. Jia, W. Zhang, C. Zhen, C. Xu, K. Tai, X. Jiang and S. Yang, *Sol. RRL*, 2020, **4**, 2000098.
7. J. Y. Ye, J. Tong, J. Hu, C. Xiao, H. Lu, S. P. Dunfield, D. H. Kim, X. Chen, B. W. Larson, J. Hao, K. Wang, Q. Zhao, Z. Chen, H. Hu, W. You, J. J. Berry, F. Zhang and K. Zhu, *Sol. RRL*, 2020, **4**, 2000082.
8. P. Hang, C. Kan, B. Li, Y. Yao, Z. Hu, Y. Zhang, J. Xie, Y. Wang, D. Yang and X. Yu, *Adv. Funct. Mater.*, 2023, 2214381.
9. C. Gao, H. Zhang, F. Qiao, H. Huang, D. Zhang, D. Ding, D. Du, J. Liang, J. Bao, H. Liu and W. Shen, *Nano Energy*, 2023, **116**, 108765.
10. A. F. Palmstrom, G. E. Eperon, T. Leijtens, R. Prasanna, S. N. Habisreutinger, W. Nemeth, E. A. Gaulding, S. P. Dunfield, M. Reese, S. Nanayakkara, T. Moot, J. Werner, J. Liu, B. To, S. T. Christensen, M. D. McGehee, M. F. A. M. van Hest, J. M. Luther, J. J. Berry and D. T. Moore, Joule, 2019, 3, 2193–2204.
11. Q. Jiang, J. Tong, R. A. Scheidt, X. Wang, A. E. Louks, Y. Xian, R. Tirawat, A. F. Palmstrom, M. P. Hautzinger, S. P. Harvey, S. Johnston, L. T. Schelhas, B. W. Larson, E. L. Warren, M. C. Beard, J. J. Berry, Y. Yan and K. Zhu, *Science*, 2022, **378**, 1295–1300.
12. D. P. McMeekin, G. Sadoughi, W. Rehman, G. E. Eperon, M. Saliba, M. T. Hörantner, A. Haghighirad, N. Sakai, L. Korte, B. Rech, M. B. Johnston, L. M. Herz and H. J. Snaith, *Science*, 2016, **351**, 151–155.
13. Y. Zhou, F. Wang, Y. Cao, J.-P. Wang, H.-H. Fang, M. A. Loi, N. Zhao and C.-P. Wong, *Adv. Energy Mater.*, 2017, **7**, 1701048.
14. Y. Yu, C. Wang, C. R. Grice, N. Shrestha and D. Zhao, *ACS Energy.*, 2017, 2 ,1177-1182.
15. J. Kim, M. I. Saidaminov, H. Tan, Y. Zhao, Y. Kim, J. Choi, J. W. Jo, J. Fan, R. Quintero-Bermudez, Z. Yang, L. N. Quan, M. Wei, O. Voznyy and E. H. Sargent, *Adv. Mater.*, 2018, **30**, e1706275.
16. H. Tan, F. Che, M. Wei, Y. Zhao, M. I. Saidaminov, P. Todorović, D. Broberg, G. Walters, F. Tan, T. Zhuang, B. Sun, Z. Liang, H. Yuan, E. Fron, J. Kim, Z. Yang, O. Voznyy, M. Asta and E. H. Sargent, *Nat. Commun.*, 2018, **9**, 3100.
17. C. Chen, Z. Song, C. Xiao, D. Zhao, N. Shrestha, C. Li, G. Yang, F. Yao, X. Zheng, R. J. Ellingson, C.-S. Jiang, M. Al-Jassim, K. Zhu, G. Fang and Y. Yan, *Nano Energy*, 2019, **61**, 141–147.
18. K. Xiao, R. Lin, Q. Han, Y. Hou, Z. Qin, H. T. Nguyen, J. Wen, M. Wei, V. Yeddu, M. I. Saidaminov, Y. Gao, X. Luo, Y. Wang, H. Gao, C. Zhang, J. Xu, J. Zhu, E. H. Sargent and H. Tan, *Nature Energy*, 2020, **5**, 870–880.
19. C. Chen, J. Liang, J. Zhang, X. Liu, X. Yin, H. Cui, H. Wang, C. Wang, Z. Li, J. Gong, Q. Lin, W. Ke, C. Tao, B. Da, Z. Ding, X. Xiao and G. Fang, *Nano Energy*, 2021, **90**, 106608.

20. R. D. J. Oliver, P. Caprioglio, F. Peña-Camargo, L. R. V. Buizza, F. Zu, A. J. Ramadan, S. G. Motti, S. Mahesh, M. M. McCarthy, J. H. Warby, Y.-H. Lin, N. Koch, S. Albrecht, L. M. Herz, M. B. Johnston, D. Neher, M. Stolterfoht and H. J. Snaith, *Energy Environ. Sci.*, 2022, **15**, 714–726.

21. Z. Zhang, J. Wang, J. Liang, Y. Zheng, X. Wu, C. Tian, A. Sun, Y. Huang, Z. Zhou, Y. Yang, Y. Liu, C. Tang, Z. Chen and C.-C. Chen, *Small*, 2023, **19**, e2303213.

22. F. Azri, A. Meftah, N. Sengouga and A. Meftah, *Solar Energy*, 2019, **181**, 372–378.

23. D. Stanić, V. Kojić, T. Čižmar, K. Juraić, L. Bagladi, J. Mangalam, T. Rath and A. Gajović, *Materials*, 2021, **14**, 6341.

24. S. Bouazizi, W. Tlili, A. Bouich, B. M. Soucase and A. Omri, *Mater. Res. Express*, 2022, **9**, 096402.

25. S. Mehmood, Y. Xia, F. Qu and M. He, *Energies*, 2023, **16**, 7438.

26. P. Srivastava, Sadanand, S. Rai, P. Lohia, D. K. Dwivedi, H. Qasem, A. Umar, S. Akbar, H. Algadi and S. Baskoutas, *Phys. Scr.*, 2022, **97**, 125004.